 doi:10.20944/preprints201804.0223.v2

Article

Preliminary Analysis of Wind Retrieval Based on GF-3 Wave Mode Images

Lei Wang [1,2,3], Bing Han [1,2,*], Xinzhe Yuan [4], Bin Lei [1,2], Chibiao Ding [1,2,3,5], Yulin Yao [6], Qi Chen [6]

[1] Key Laboratory of Technology in Geo-Spatial Information Processing and Application Systems, Institute of Electronics, Chinese Academy of Sciences, Beijing 100190, China; wanglei162@mails.ucas.edu.cn (L.W.); leibin@mail.ie.ac.cn (B.L.); cbding@mail.ie.ac.cn (C.D.);
[2] Institute of Electronics, Chinese Academy of Sciences, Beijing 100190, China;
[3] School of Electronic, Electrical and Communication Engineering, University of Chinese Academy of Sciences, Beijing 100049, China
[4] National Satellite Ocean Application Service, State Oceanic Administration, Beijing 100081, China; harley_yuan@mail.nsoas.org.cn
[5] National Key Laboratory of Microwave Imaging Technology, Institute of Electronics, Chinese Academy of Sciences, Beijing 100190, China
[6] China Centre for Resource Satellite Data and Application, Beijing 100094, China; yaoyulin886@163.com (Y.Y.), chenq_cn@163.com (Q.C.);
[*] Correspondence: han_bing@mail.ie.ac.cn; Tel.: +86-10-5888-7208 (ext. 8956)

Abstract: In this paper, we analyze the measurements of the normalized radar cross-section(NRCS) in Wave Mode for Chinese C-band Gaofen-3(GF-3) synthetic aperture radar (SAR). Based on 2779 images from GF-3 quad-polarization SAR in Wave Mode and collocated wind vectors from ERA-Interim, we verify the feasibility of using ocean surface wind fields and VV-polarized NRCS to perform normalized calibration. The method uses well-validated empirical C-band geophysical model function (CMOD4) to estimate the calibration constant for each beam. The Amazon rainforest experiment results show that the accuracy of obtained calibration constant meets the requirements. In addition, the relationship between cross-pol NRCS and wind vectors is discussed. The cross-pol NRCS increases linearly with wind speed and it has an approximate cosine modulation with the wind direction when the wind speed is greater than 8m/s. The cross-polarized system noise floor is low enough to ignore it in wind retrieval. Furthermore, we also investigate the properties of the polarization ratio, denoted PR, and show that it is dependent on incidence angle and azimuth angle. Two empirical models of the PR are fitted, one as a function of incidence angle only, the other with additional dependence on azimuth angle. Assessments show that the σ_{VV}^0 retrieved from new PR models as well as σ_{HH}^0 is in good agreement with σ_{VV}^0 extracted from SAR images directly. And it is also shown that considering the azimuth angle can improve polarization conversion accuracy.

Keywords: Gaofen-3; SAR; Wave Mode; calibration constants; cross-pol; noise floor; polarization ratio;

1. Introduction

With the continuous depletion of global petroleum energy, the development and utilization of clean wind energy have become a hot topic in recent decades. Offshore wind energy is the focus of research due to the vast area of marine resources. Measurements of offshore wind information also contribute to oil spill monitoring, weather forecasting and understanding of air-sea interactions [1-3]. Spaceborne active microwave scatterometer such as QuickSCAT and ASCAT have provided mature wind products for National Oceanic and Atmospheric Administration(NOAA) [4,5]. However, the spatial resolution of the wind products acquired by scatterometer (12.5km~25km) cannot applied to the retrieval of the fine scale ocean surface wind fields [6]. Synthetic aperture radar (SAR) has excellent characteristics such as imaging at all-weather conditions and high spatial

resolution. It is widely used in military, economics, and science, and plays an important role in the retrieval of ocean surface wind fields, especially for C-band (~5.3GHz) SAR [7].

Numerous studies have revealed that ocean surface normalized radar cross-section (NRCS) obtained from C-band SAR is mainly dominated by resonant Bragg backscattering at the wavelength of centimeter scale [8-10]. This scale roughness is predominantly influenced by local wind and therefore ocean wind information may be extracted from SAR images [11]. In recent decades, several empirical geophysical model functions (GMFs), such as CMOD4 [12], CMOD_IFR2 [13], CMOD5 [14], CMOD5.N [15] have been proposed to perform ocean surface wind fields retrieval. These GMFs relate the NRCS to the incidence angle, wind speed at a height of 10m above sea level, and azimuth angle (radar look angle with respect to wind direction). Not only scatterometer, such as QuickSCAT [16,17] and ASCAT [18], they can also accurately retrieve the wind speed from SAR image (within about 2m/s), e.g., ENVISAT [19], RADARSAT-1/2 [20-22] and Sentinel-1A/B [23]. However, such GMFs are only suitable for VV-polarized NRCS, no similar models exist to retrieve wind speed from images in HH-polarization. Therefore, it is necessary to convert HH-polarized NRCS to VV-polarization using polarization ratio (PR), denote as $PR = \sigma_0^{VV}/\sigma_0^{HH}$ [linear units], before retrieving wind speed [24-28]. In traditional research, it is generally believed that the PR is only relevant to incidence angle [24]. Recent studies in [27,28] show that the PR is also dependent on speed and azimuth except incidence angle. These results reveal that different satellites have their own optimal PR and GMF. Thus, the choice of suitable hybrid models before retrieving wind fields is critical for Gaofen-3 satellite [29].

Recent several decades, wind speed retrieval from cross polarized (cross-pol) NRCS has become a research focus due to the saturation of co-pol data at high wind speed. Some studies of cross-pol images have been done for RADARSAT-2 quad-polarization and dual-polarization [30-35]. The cross-pol NRCS is independent on incidence angle and wind direction, and increases linearly with wind speed for quad-polarization mode which has a low noise floor (about -36dB). Since the dual-polarization of RADARSAT-2 has a high noise floor, it is necessary to remove the influence of noise before retrieving wind speed using cross-pol NRCS. Moreover, Huang et al. [36] conduct an evaluation on cross-pol NRCS in Sentinel-1 IW mode and propose a wind retrieval algorithm related to incidence angle and wind direction. The above studies show that the cross-pol NRCS has potential to retrieve high wind speeds, e.g. hurricanes and typhoons.

The accuracy of the retrieved wind vector is strongly affected by the NRCS absolute radiometric calibration accuracy. Accurate wind speed can be obtained from refined NRCS. Therefore, it is possible to assess the accuracy of the calibration by using GMFs and known wind information. Horstmann et al. [37] propose a method for estimating ERS SAR calibration constant using c-band models and ocean surface wind fields. Stoffelen et al. [38] obtain an accurate calibration of a scatterometer over the ocean using CMOD4 and wind fields from European Centre for Medium-Range Weather Forecasts (ECMWF). This method achieves a calibration accuracy of 0.1 dB. Verspeek et al. [39] propose an estimating correction tables based on CMOD5.N to improve ASCAT wind retrieval. Zhu et al. [40] use Numerical Ocean Calibration (NOC) to calibrate HY-2 SCAT and its retrieved winds are in good agreement in winds from ECMWF.

The Gaofen-3 (GF-3) satellite which was launched on 10 August by the China Academy of Space Technology (CAST) is the first C-band multi-polarization SAR with a highest resolution of 1m in China. It has characteristics such as high resolution, large coverage, long-life operation and multiple imaging modes, including Wave Mode [41]. To date, some preliminary evaluations of ocean application have been carried out. Shao et al. [42] collect 244 Stander Stripmap (SS) and Quad-Polarization Stripmap (QPSI and QPSII) mode images to complete wind and wave retrieval firstly. In [29] Wang et al. validate the GF-3-derived winds against NDBC measurements using 37 GF-3 SAR scenes in SS, QPSI, QPSII, FSI and NSC modes. Ren et al. [43] conduct a comprehensive analysis for QPSI and QPSII mode data in each polarization. Several empirical algorithms for significant wave height in Wave Mode data and wind retrieval from cross-polarization in typhoons are also discussed in [44,45], which uses GF-3 images acquired in Global Observation (GLO) and Wide ScanSAR (WSC) mode .

Preprints (www.preprints.org) | NOT PEER-REVIEWED | Posted: 18 April 2018 doi:10.20944/preprints201804.0223.v2

The remainder of this paper is organized as follows. Section 2 describes the GF-3 Wave Mode SAR images and the other validated data, including ECMWF ERA-Interim re-analysis wind fields and Amazon rainforest images. Methodologies for correcting calibration constants, fitting PR models and cross-pol wind speed retrieval formula are introduced in section 3. Section 4 shows results of calibration, polarization conversion and wind speed retrieval accuracy. Finally, discussion and conclusion are presented in section 5.

2. Description of Datasets

2.1. GF-3 SAR Wave Mode images

An experiment in [46] shows that GF-3 images can meet the satellites' polarimetric accuracy requirements, and the channel imbalance is 0.5dB as well as a crosstalk accuracy of -35dB. In this study, we totally collect 5336 GF-3 Level-1A Wave Mode data between March 1, 2017 and December 31, 2017 over the Pacific, Atlantic and Indian Ocean. The task of Wave Mode is to observe ocean surface waves over open ocean, and the size of Wave Mode image is about 5km × 5km every 50 km along the orbit. The biggest difference between Wave Mode and other modes is the incidence angle. Although the incidence angle coverage of Wave Mode is 20° to 50°, it only fixes in 28 beams with a narrow data acquisition window about 0.4°. This results in discrete incidence angle for images between different beams, e.g. incidence angle of beam 189 is about $21.5 \pm 0.2°$ and the incidence angle of beam 190 is about $23.7 \pm 0.2°$ etc. [44,41]. The parameter details of Wave Mode products are listed in Table 1.

Table 1. Parameters for GF-3 Wave Mode.

Imaging mode	Incidence angle (°)	Polarization	Resolution (m)	Swath (km)
WAV	20-50	HH+VV+HV+VH	10	5

The Level-1A products are single look complex (SLC) images. Let I represent real channel of images, Q as the imaginary channel. The equation of NRCS is as follow.

$$\sigma^0 = 10 * lg\left[\left(\frac{I}{32767} * Qualify\right)^2 + \left(\frac{Q}{32767} * Qualify\right)^2\right] - K\_const \quad (1)$$

Where σ^0 is the NRCS in dB, Qualify is the QualifyValue in product description xml of GF-3, and K_const is the calibration constant.

Several studies indicate that wind speed can only be retrieved from pure ocean SAR images which are free of sea features not due to the local wind, e.g. ice and slicks [2,47]. To screen out the Wave Mode images which are not affect by features due to slicks or ocean phenomenon, we use homogeneity check procedures proposed in [44] before experimental study. Wang et al. [44] show that the Wave Mode normalized variance (*cvar_vv*) computed from VV-polarization images can be used as a standard for verifying image homogeneity. Here, we also choose the images which with $1.1 < cvar\_vv < 1.6$ for developing and validating wind retrieval algorithms. The parameter of homogeneity test is defined as

$$cvar\_vv = var\left(\frac{I-\bar{I}}{\bar{I}}\right) \quad (2)$$

where $\bar{I}$ is the mean intensity of GF-3 Wave Mode image in VV-polarization. In addition, the saturated co-polarization NRCS can also affect the experimental results. Hence, we only use the SAR images with 0% saturation coefficient.

After the above two preprocessing processes, a total of 3926 GF-3 Wave Mode images are selected from 5336 images. The result shows that the small incidence angle (in-angle < 36°) co-pol data is almost saturated for the 10 months in 2017, according to product description xml. Therefore, the analyzed incidence angle of this paper is only from 39° to 47°. The detail information of data distribution is shown in the Figures 1-3 below. To guarantee the validity of experiment, we first divide the whole data into training and testing set randomly. Then, adjusting a small amount of data

Preprints (www.preprints.org) | NOT PEER-REVIEWED | Posted: 18 April 2018 doi:10.20944/preprints201804.0223.v2

artificially so that both set can cover full range of incidence angles, azimuth angles and wind speeds. We finally choose 2779 match-ups as training set and other 1147 samples as testing set.

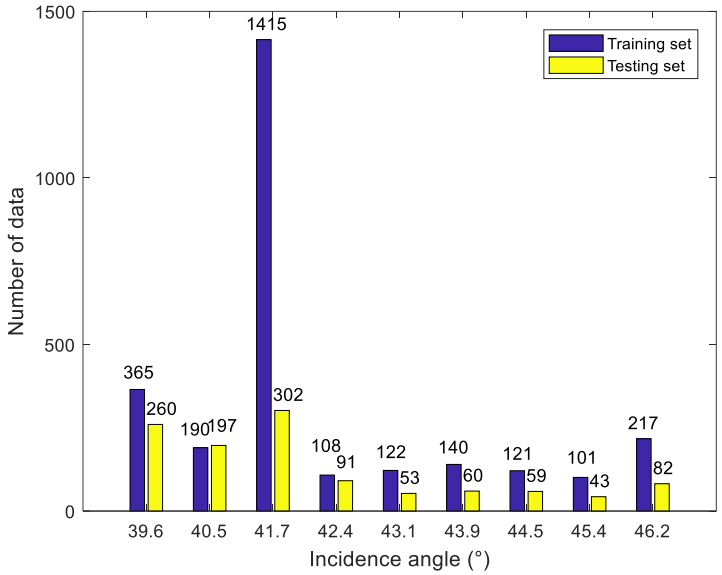

Figure 1. Incidence angle histogram of the data set

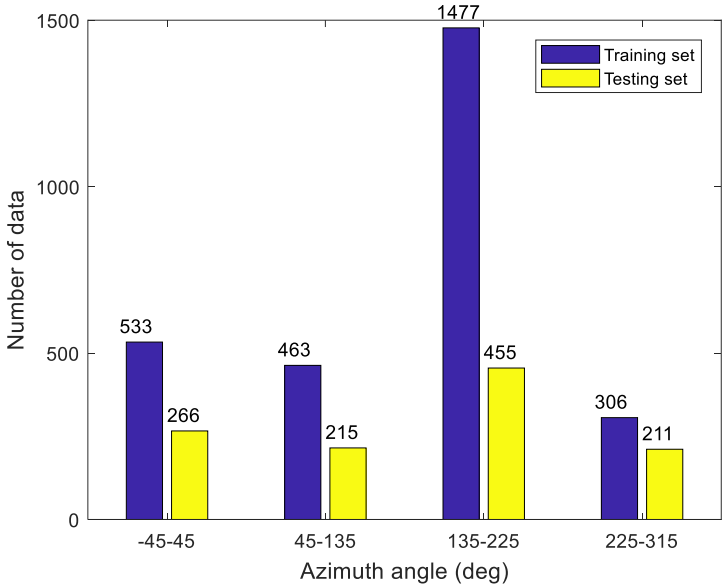

Figure 2. Azimuth angle histogram of the data set

Preprints (www.preprints.org) | NOT PEER-REVIEWED | Posted: 18 April 2018 doi:10.20944/preprints201804.0223.v2

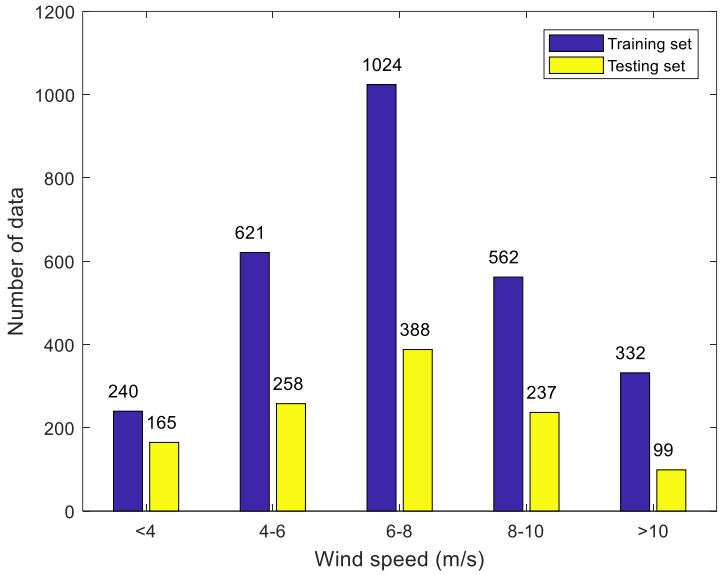

Figure 3. Wind speed histogram of the data set

2.2. Other Validation Sources

ERA-Interim is a global atmospheric re-analysis from 1979, continuously updated in real time, provided by ECMWF which is an independent intergovernmental organization supported by 34 states. The re-analysis wind field data is widely used in retrieval and comparison of wind vectors [12-15]. In this study, the spatial resolution of wind products downloaded on [48] is 0.125°×0.125° (lat/lon), and the temporal resolution is 6h (00:00, 06:00, 12:00, 18:00).

The Amazon rainforest has excellent temporal and spatial stability as a radar distributed target calibration source. And its maximum backscatter deviation is about 0.2dB. There have been numerous researches using the Amazon rainforest for radar radiometric calibration [49]. Here, we use beam 205 SAR images which have a large number of data and corresponding beam of the Amazon rain forest Wave Mode SAR images to validate the feasibility of ocean calibration.

3. Experiments and Analysis

For the 2779 training data and 1147 testing data, we make a 512 × 512 pixel boxcar in each center of Wave Mode images to average the NRCS in co-polarization (HH and VV), so that the NRCS spacing is about 5km. As mentioned in section 2, the wind fields' spatial resolution as about 12.5km × 12.5km. To improve the match accuracy between wind fields and SAR images, we interpolate the wind field time to 1h using a cubic spline interpolation and use bilinear interpolation to interpolate four velocity components near the center point to the center. And the time difference between SAR image and wind vector is within 30min.

3.1. Calibration Method Based on Ocean Wind

As shown in equation (1), the NRCS in dB is linear with calibration constant. It provides a possibility for using the wind field and GMFs to retrieve the calibration constant. We can obtain simulated NRCS in VV-polarization using CMOD4 and wind vectors. Then the difference between simulated NRCS and the value extracted from corresponding image directly is the stimulated calibration constant. This method requires plentiful fitted data to ensure the accuracy of results and each beam has their own calibration constant. Therefore, we use match-up data of 41.7° incidence angle (beam 205) in the training set to verify the calibration method. To guarantee the reliability of the calibration method, we only select data with wind speed higher than 4m/s due to the inaccuracy of CMOD4 at low wind speed. Moreover, the distribution of wind speed and direction in the

Preprints (www.preprints.org) | NOT PEER-REVIEWED | Posted: 18 April 2018 doi:10.20944/preprints201804.0223.v2

experimental data set also affects the calculation of calibration constant. Hence, we first split the training set into wind speed bins of size 2m/s and azimuth bins of size 90°. Then, let each speed bin has roughly the same amount of data and filter data in each speed bin so that the distribution of azimuth angle is uniform. Finally, we obtain 901 uniform match-up data to implement the calibration method. Figure 4 shows the relationship between simulated NRCS by CMOD4 and values obtained directly from VV polarized images.

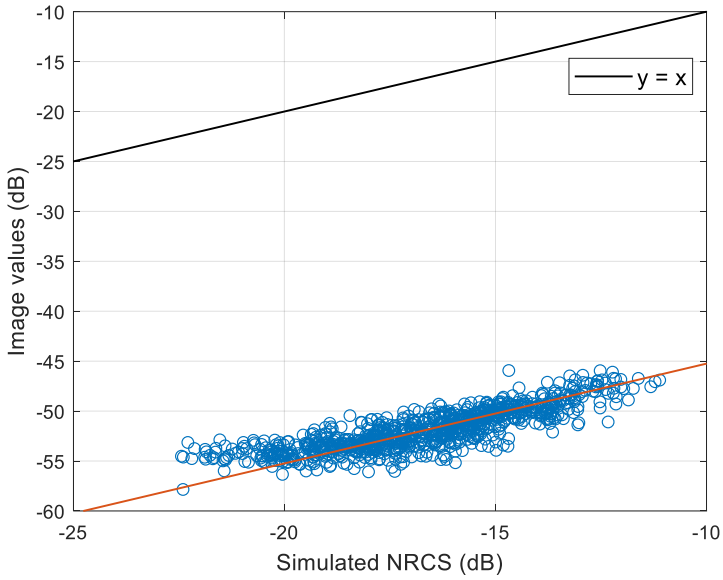

Figure 4. Relationship between simulated NRCS and values obtained directly from images

The solid black line in Figure 4 is the bisector of the axis quadrant and the solid red line is the fitting curve of the training data with the same slope. As shown in the Figure, the difference between the simulated NRCS and image values is a constant. We find the best calibration constant using a minimum squared-error criterion. And the calibration constant calculated is 29.486. The calibration constant of beam 205 given by China Centre for Resources Satellite Data and Application is 29.665. The difference between alpha-testing constant and calculated constant is within 0.2dB. It shows the method has a good performance.

3.2. Analysis of Wind sensitivity for Cross-pol NRCS

The cross-pol backscattering signal-to-noise ratio (SNR) of ocean surface is much weaker than co-pol signal. Therefore, it is necessary to compare cross-pol NRCS with the system noise floor before wind retrieval [36]. The Institute of Electronics, Chinese Academy of Sciences provides a ground system processing technology for GF-3 satellite, and we can obtain the noise gain coefficient of Wave Mode. Due to the limited number of products with system noise gain coefficient, we only collect 138 sets of match-ups with noise floor. Figure 5 shows the HV-polarized NRCS as a function of ERA-Interim re-analysis wind speed. And the system noise floor is also plotted.

As illustrated in Figure 5, the HV-polarized noise floor of Wave Mode is about -40 dB. It is sufficiently low, and we can ignore the impact of noise floor when retrieving wind speed using HV-polarized NRCS. The relationship between the NRCS σ_{HV}^0 after calibration correction and wind speed is shown in Figure 6. Different colors represent different incidence angles. As previous research, the σ_{HV}^0 is intendent on incidence angle and exists obvious linear relationship with wind speed. The black solid line is obtained using a non-linear least-squares method, and the formulation is

$$\sigma_{HV}^0 = 0.6359 * U_{10} - 36.1384 \quad (3)$$

where σ_{HV}^0 is the HV-polarized NRCS in dB and U_{10} is the wind speed at 10m.

Preprints (www.preprints.org) | NOT PEER-REVIEWED | Posted: 18 April 2018 doi:10.20944/preprints201804.0223.v2

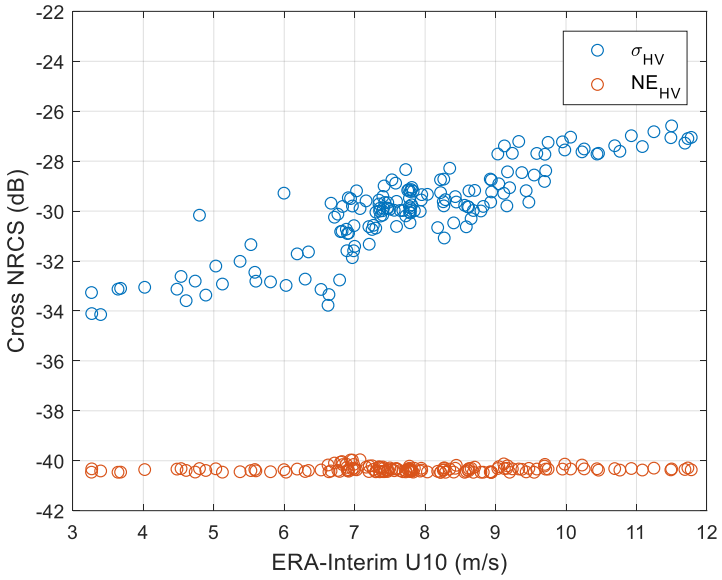

Figure 5. HV-polarized NRCS and noise floor versus wind speed

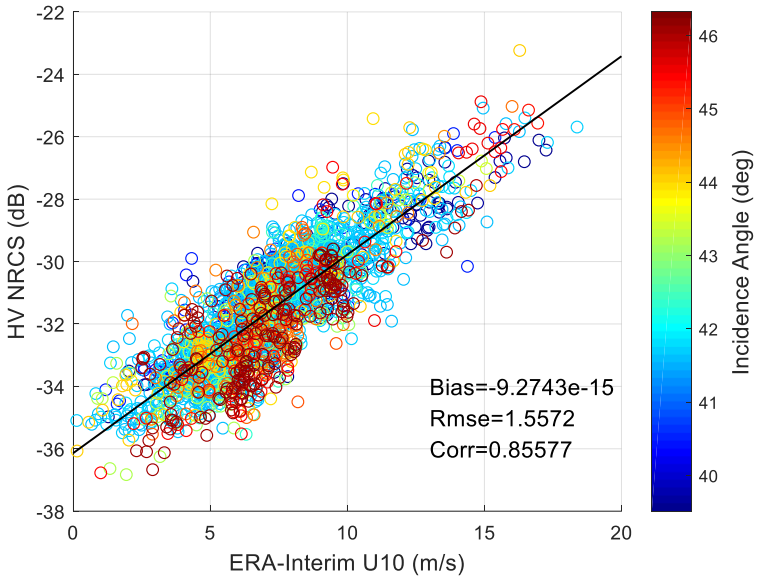

Figure 6. Relationship between NRCS and wind speed (different colors represent different incidence angle)

The wind retrieval algorithm of cross-pol NRCS in this study is similar to the formula in [30,31,43]. The retrieved wind speed using (3) has an RMSE of 1.56 m/s and a correlation coefficient of 0.86. This indicates that the accuracy of cross-pol wind retrieval algorithm is sufficiently high, and we can retrieve wind speed from cross-pol NRCS directly without inputting wind direction and incidence angle.

Preprints (www.preprints.org) | NOT PEER-REVIEWED | Posted: 18 April 2018 doi:10.20944/preprints201804.0223.v2

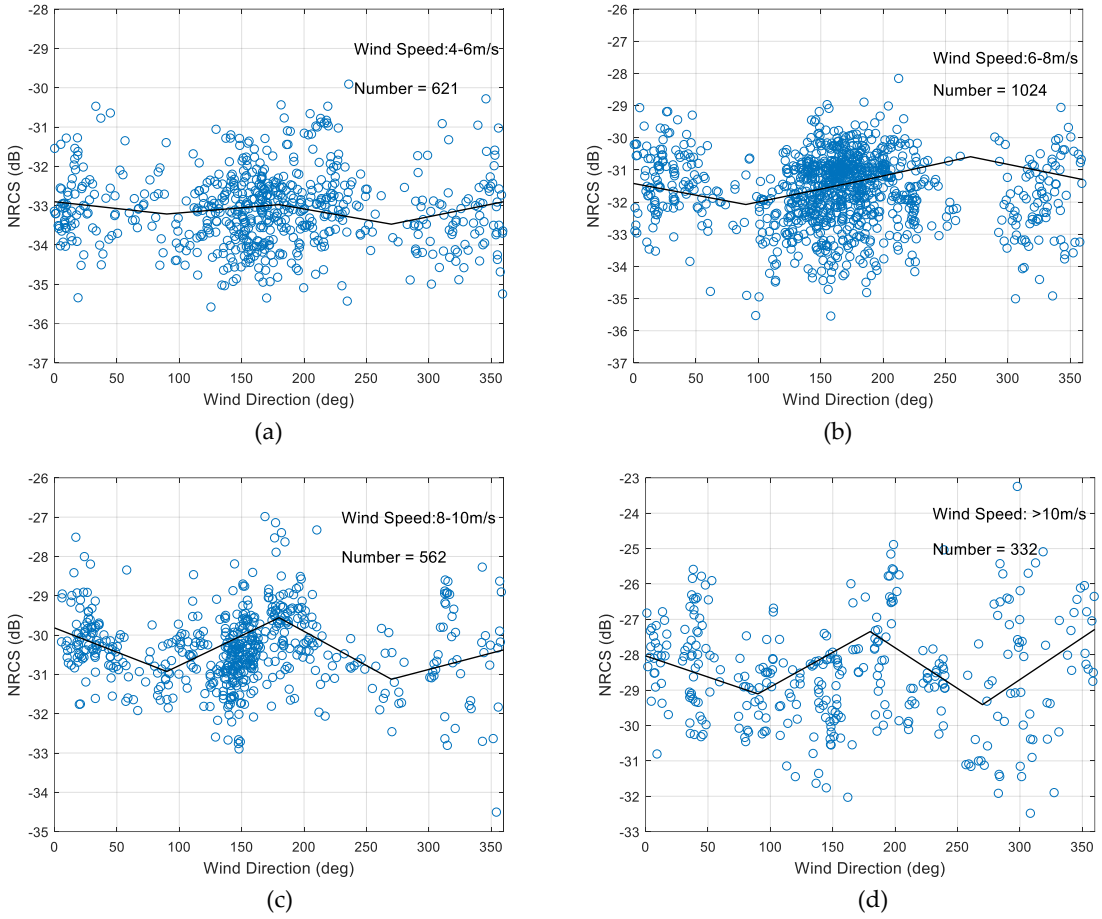

Figure 7. Relationship between cross-pol NRCS and azimuth angle

We also give an assessment of relationship between cross-pol NRCS and azimuth angle at different winds. The training set is divided into 4-6m/s, 6-8m/s, 8-10m/s, >10m/s four sets, respectively, according to wind speed, and the variation trend of σ_{HV}^{0} with azimuth angle is shown in Figures 7(a)-(d). The black solid line is the connection between the mean of the four main wind directions, e.g. upwind ($\phi = 0$), downwind ($\phi = 180$) and crosswind ($\phi = 90$, $\phi = 270$). When speed is higher than 8m/s, the σ_{HV}^{0} shows approximately cosine relationship with azimuth angle. This property is consistent with GF-3 QPSI and QPSII mode data in [43]. Therefore, the influence of wind direction should be considered when retrieving high wind speeds, e.g. hurricanes and typhoons.

3.3. Development of PR Models

Figure 8 shows the relationship between PR and incidence angle as well as wind speed based on 2779 training data. Different colors represent the different wind speeds. And the solid black line is formed by connecting the mean values of PR in each beam. The PR increase rapidly with increasing incidence angle as previous reported. In each incidence angle bin, the distribution of wind speed is random. Therefore, it can be considered that there is a weak correlation between wind speed and PR of GF-3 Wave Mode.

Preprints (www.preprints.org) | NOT PEER-REVIEWED | Posted: 18 April 2018 doi:10.20944/preprints201804.0223.v2

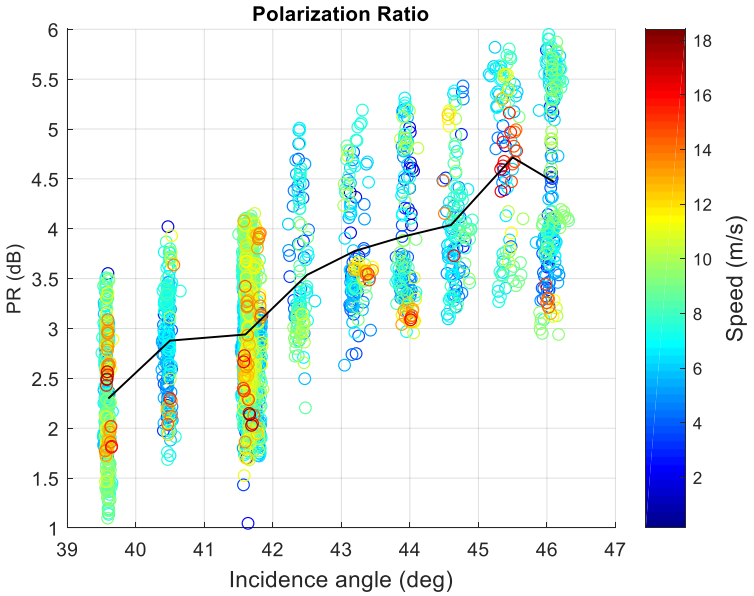

Figure 8. PR as a function of incidence angle (different colors represent different wind speed)

Here, we first fit a PR mode which is only related to the incidence angle and define it as Model 1. The formulation is

$$PR = Aexp(B\theta) + C \quad (3)$$

where PR is in linear unit, and A, B as well as C are coefficients fitted by a nonlinear least squares method given in Table 2.

Table 2. Coefficients of Model 1

Cofficient	Fitted valuses
A	0.02985
B	0.09727
C	0.305

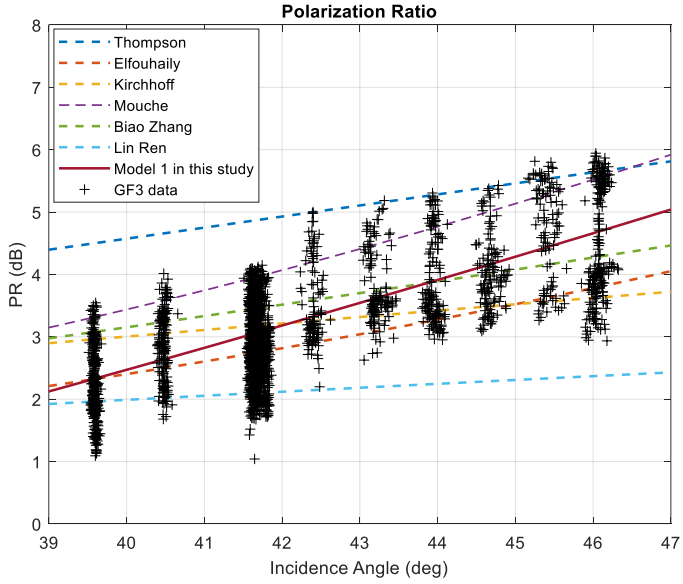

Figure 9. Comparison between Model1 and other PR models

Preprints (www.preprints.org) | NOT PEER-REVIEWED | Posted: 18 April 2018 doi:10.20944/preprints201804.0223.v2

Comparison with other PR models introduced in section 1 is shown in Figure 9. PR models of Biao Zhang and Mouche [27,28] are also an exponential of the incidence angle like us, but with different coefficients. The formulation of other researchers [24,43] is expressed as PR

$$PR = (1 + 2tan^2\theta)^2/(1 + \alpha tan^2\theta)^2 \quad (4)$$

where α is an adjustable parameter. As illustrated in Figure 5, the Model 1 we fitted is closest to the mean of GF-3 Wave Mode.

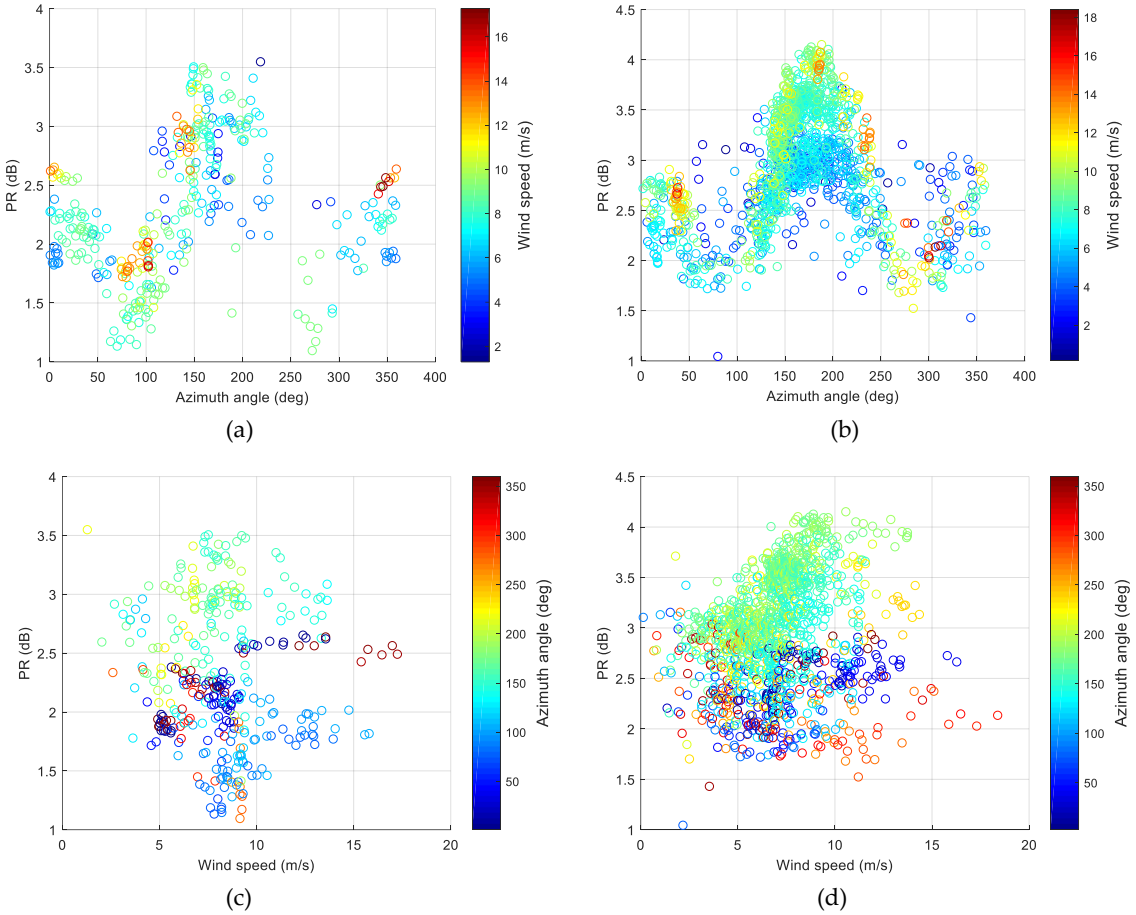

Figure 10. (a) and (b) represent the variation between PR and azimuth angle and different color shows different wind speed. (c) and(d) show the relationship between PR and wind speed. Different color represents different azimuth. (a) and (c) are at incidence angle 39.6°. (b) and (d) are at incidence angle 41.6°.

To give a more comprehensive PR analysis for GF-3 Wave Mode data, we also study the relationship between PR and azimuth angle and observe a similar characteristic as in [28]. The variation of PR with azimuth angle is shown in Figures 10(a), (b), (c) and (d) at the incidence angle of 39.6° and 41.7° (beam 202 and 205), respectively. It is obviously that there is an approximately cosine relationship between PR and azimuth angle like the characteristic between NRCS and azimuth angle. The maximum of PR is observed in downwind direction ($\phi = 180°$), a secondary maximum is appeared in upwind direction ($\phi = 0°$) and the minimum values are in crosswind ($\phi = 90°$). This is slightly different from NRCS which appears maximum in upwind and secondary maximum value in downwind. In addition, the PR tends to increase with the increase of wind speed (<10m/s) in the downwind, while it is independent with wind speed in other wind direction. However, we cannot conclude that the PR increases linearly with wind speed in the downwind due to insufficient high wind speed data in downwind. Hence, we temporarily ignore the influence of wind speed and fit training set using nonlinear least squares, deriving Model 2 for PR with additional dependence on azimuth angle. The Model 2 is assumed to follow

Preprints (www.preprints.org) | NOT PEER-REVIEWED | Posted: 18 April 2018 doi:10.20944/preprints201804.0223.v2

$$PR(\theta,\phi) = C_0(\theta) + C_1(\theta)\cos\phi + C_2(\theta)\cos 2\phi \quad (5)$$

where ϕ is azimuth angle and the PR is in linear unit. In each azimuth angle, the relationship between PR and incidence angle is also defined as exponential function.

$$PR_\phi(\theta) = A_\phi exp(B_\phi\theta) + C_\phi \quad (6)$$

The coefficients C_i(i = 0, 1, 2) can be calculated by the method of undetermined coefficients, and the formulas are as follow

$$C_0(\theta) = \big(P(\theta,0) + P(\theta,\pi) + 2P(\theta,\pi/2)\big)/4 \quad (7a)$$

$$C_1(\theta) = \big(P(\theta,0) - P(\theta,\pi)\big)/2 \quad (7b)$$

$$C_2(\theta) = \big(P(\theta,0) + P(\theta,\pi) - 2P(\theta,\pi/2)\big)/4 \quad (7c)$$

We first fit the coefficients (A_ϕ, B_ϕ, C_ϕ) of three main directions (upwind, downwind, crosswind) using a nonlinear least squares method. Then using them to obtain coefficients C_i. Table 3 shows the fitting results.

Table 3. Coefficients of Model 2

Coefficients	Fitted values
A_0	0.1715
B_0	0.06242
C_0	-0.4342
$A_{\pi/2}$	0.9331
$B_{\pi/2}$	0.03606
$C_{\pi/2}$	-2.44
A_π	0.000393
B_π	0.1912
C_π	1.119

4. Validation and Results

4.1. Results of Ocean Calibration

The alpha-testing calibration constant is derived from system bandwidth and antenna pattern and has not been verified by field calibration. Therefore, we collect 7 GF-3 Wave Mode SAR images of the Amazon rainforest area in beam 205 to verify the calibration constant obtained in section 3.2. The distribution of Amazon rainforest γ is shown in Figure 11.

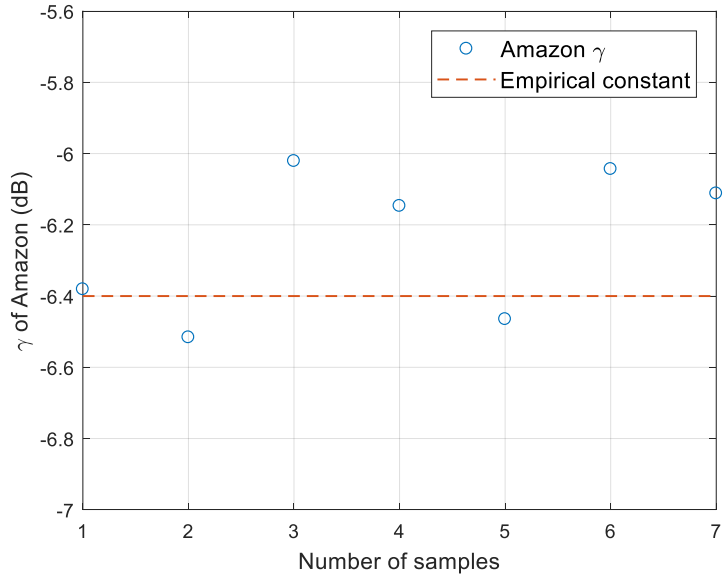

Figure 11. Distribution of Amazon rainforest γ

Preprints (www.preprints.org) | NOT PEER-REVIEWED | Posted: 18 April 2018 doi:10.20944/preprints201804.0223.v2

As described in [49], the γ of Amazon rainforest can be considered as a constant value due to the stability of this area. The γ can be characterized as

$$\gamma = \sigma^0/\cos\theta = \beta^0 \tan\theta \quad (8)$$

where γ, σ^0 and β^0 are forms of the backscattering coefficient and radar brightness. It is generally accepted that the γ of Amazon rainforest changes around -6.4dB within 0.2dB. And the distribution of γ from RADARSAT-1 is $-6.47 \pm 0.71dB$ according to [49]. Figure 9 illustrates the γ of GF-3 Wave Mode data in beam 205 is around $-6.4 \pm 0.4dB$. Therefore, it can be demonstrated that the calibration constant obtained using the ocean calibration is sufficiently accurate. And if we acquire enough data, the calibration constant can be obtained continuously using the ocean surface wind fields, which provides the possibility for normalized calibration.

Based on the obtained calibration constant, we use GMFs to complete wind speed retrieval on beam 205 data of testing set. Figures 12 (a)-(d) show the comparison between ERA-Interim wind speeds and retrieved wind speeds using CMOD4, CMOD_IFR2, CMOD5, CMOD5.N , respectively.

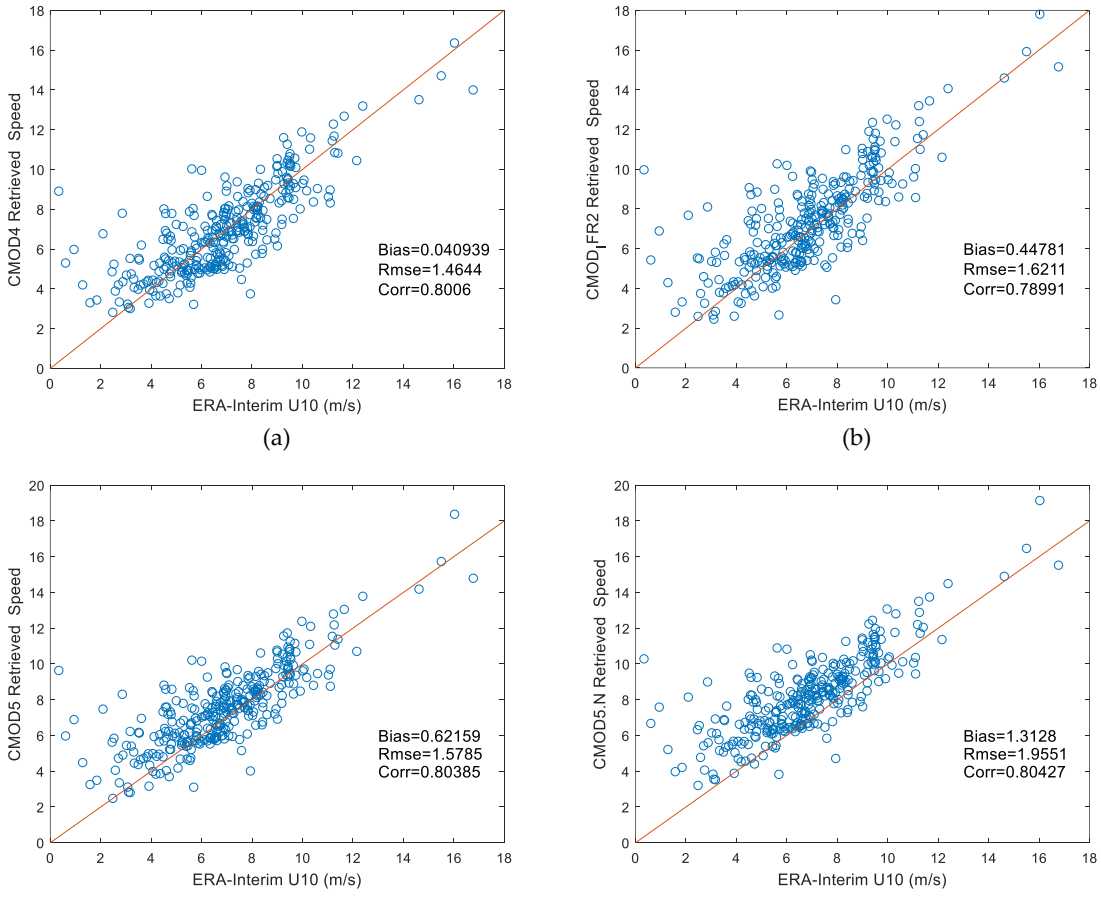

Figure 12. Comparison of ERA-Interim U10 with SAR-derived wind speeds

As demonstrated in Figures 12, the estimated calibration constant can be well applied to SAR image wind speed retrieval and the RMSE of retrieved speed is less than 2m/s. However, large inaccuracies may occur in wind retrieval using GMFs when the wind speed is lower than 2m/s. The accuracy of retrieved speed using CMOD4 is higher than others at low to moderate wind speeds and its RMSE is 1.46m/s. We cannot verify the advantages of CMOD5 due to the lack of data at high wind speeds.

Preprints (www.preprints.org) | NOT PEER-REVIEWED | Posted: 18 April 2018 doi:10.20944/preprints201804.0223.v2

4.2. Validation of Wind Retrieval for Cross-polarization

We use the testing set to evaluate the performance of cross-polarization wind retrieval formula in this paper compared with algorithms in [30,31,43]. The RMSE and bias between ERA-Interim U10 and retrieved speed is listed in Table 4.

Table 4. Comparison of Wind Speed Retrieval Algorithm

	Rmse (m/s)	Bias (m/s)
Mine	1. 5046	-0.1758
Vachon	1.6063	0.2026
Zhang	1.6271	-0.0273
Ren	2.0505	-1.1759

As shown in Table 4, the algorithm fitted in this paper has the optimal inversion accuracy with RMSE 1.5 m/s. The formula proposed by Zhang has the smallest bias with -0.027 m/s. The retrieval result is slightly poor when the formula fitted by QPSI and QPSII data is applied to the Wave Mode data, which has RMSE with 2.05 m/s and bias with -1.18 m/s.

4.3. Validation of PR Models using Testing Set

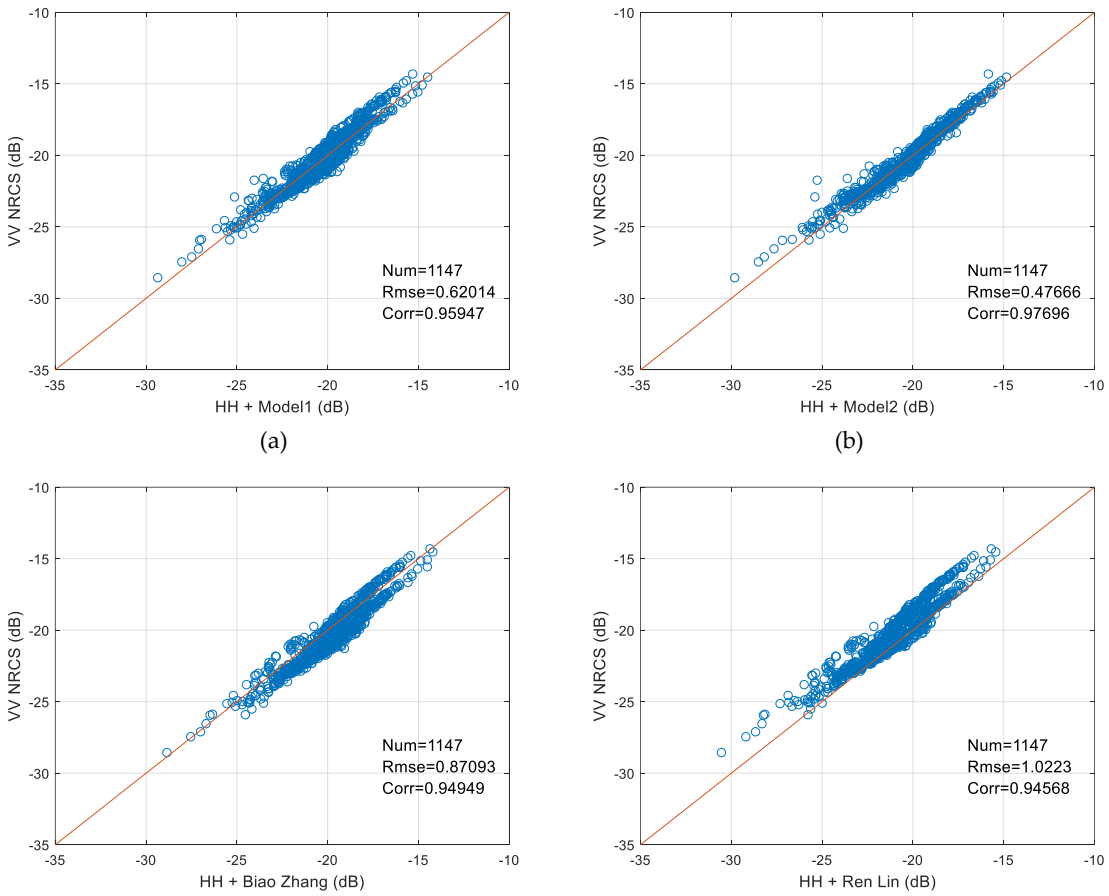

Figure 13. Comparison of four different PR models based on testing set

To evaluate the performance of two fitted PR models, we test the models in testing set and compare two models with different models in [27,43]. PR model proposed by Zhang in [27] is a

 doi:10.20944/preprints201804.0223.v2

function of incidence angle as well as wind speed and mode fitted by Ren in [43] is dedicated to GF-3 QPSI and QPSII mode data.

Figures 13(a)-(d) illustrate the comparison of four PR models. The abscissa of figure is retrieved NRCS by PR model and the ordinate is NRCS from SAR image in VV polarization. Figures also show the root-mean-square error (RMSE) and correlation coefficient for each model. It is shown that two models used in this study are in better agreement with Wave Mode data. And Model 2 which consider the influence of wind direction has a smaller RMSE (0.4767dB) and larger correlation coefficient (0.977). In addition, Figure 8(d) shows the PR model proposed for GF-3 QPSI and QPSII mode cannot be well used in Wave Mode data. The retrieved NRCS is generally lower than observation. There may be two reasons for this result. First, the imaging bandwidth and system noise floor of two operating modes are different. These may affect the observation of NRCS. In addition, the PR model in Figure 8(d) is mainly fitted by data with incidence angles between 35°-38°, while PR models in this study are mainly applicable to data with incidence angles greater than 39°, due to the lack of small incidence data.

5. Discussion and Conclusion

In this paper, we conduct a preliminary analysis of SAR images in Wave Mode for GF-3 satellite. 2779 GF-3 Wave Mode NRCS and wind vectors for the corresponding location are collected as training set and additional 1147 match-ups are as testing set. To reduce the effect of speckle noise and improve the matching precision of the data set, we first sample the SAR NRCS from 10m pixel spacing to 5km, then we interpolate the wind field interval to 1h and obtain the wind vectors of the center of each SAR image using bilinear interpolation.

A simple method for absolute radiometric calibration using ocean surface wind fields and CMOD4 is introduced and tested. Due to the linear relationship between NRCS and calibration constant, we can obtain an estimator of calibration constant by calculating the difference between the simulated NRCS and image value. Since the calibration constant given by China Centre for Resources Satellite Data and Application is only calculated by combing system bandwidth and antenna pattern, we also verify the constant using Amazon rainforest data. The result shows the Amazon rainforest γ obtained using estimated calibration constant is in good agreement with empirical γ. This normalized calibration method provides a more convenient and affordable way for future absolute radiometric calibration. It saves the expensive cost of calibration using corner reflector and can obtain an accurate calibration constant continuously.

We also investigate the relationship between cross-pol images of Wave Mode and system noise floor, wind vectors and satellite geometry parameters. The experiment indicates that the system noise floor of cross polarization is about -40dB and we can ignore it when retrieving wind speed using cross-pol NRCS. There is a clear linear relationship between cross-pol NRCS and wind speeds and the cross-pol NRCS is intendent on incidence angle. As the wind speed increase, the cross-pol NRCS is more affected by azimuth angle. It presents approximately cosine relationship with azimuth angle when speed is higher than 8 m/s. Therefore, it is necessary to consider the azimuth angle when retrieving high wind speed in the future.

The PR of Wave Mode is not only dependent on incidence angle but also modulated by the azimuth angle. Its first maximum corresponds to downwind direction, the second in the upwind, and two minima appear in the crosswind direction. Moreover, when speed is lower than 10m/s, the PR presents a linear increase trend with wind speed in the downwind while it is independent on wind speed in other wind directions. Therefore, we fit two PR models which are suitable for large incidence angle using training set. The first is only dependent on incidence angle (Model 1) and the other one adds additional azimuth angle variable (Model 2). The results of two models on the testing set show that the PR models fitted in this paper are superior to models given in previous studies [24-28,43]. The Model 2 has higher polarization conversion accuracy than Model 1, with RMSE 0.477dB and correlation coefficient 0.977.

To date, GF-3 satellite only operates for more than one year and is still in the preliminary application stage. Since SAR images before February 2017 lack saturation coefficients and it cannot

confirm whether the data is saturated or not, images used in this paper are all collected after March. Furthermore, most of the data in the experiment is from the east Pacific Ocean near North America on September, October and November. The three-month data is mainly concentrate on the beam 202 (39.6°) and 205 (41.7°). Therefore, the beam 205 is the main part of the data. Moreover, the collected SAR images whose incidence angles are lower than 39°(lower than beam 200) are all saturated and cannot be used. These cause the non-uniformity of the data in incidence angle distribution. In the future work, we will collect more Wave Mode images which cover a wide range of incidence angles and wind speeds in high wind conditions. Additionally, we will further research the reasons for different polarization ratios under different operating modes to find a uniform PR model for GF-3 satellite.

Acknowledgments: The authors thank the National Satellite Ocean Application Service and China Centre for Resources Satellite Data and Application for providing GF-3 Wave Mode SAR data and calibration constants. And the wind fields are downloaded from ECMWF EAR-Interim http://apps.ecmwf.int/datasets/data/interim-full-daily/levtype=sfc/ for free. We would also like to thank Jingfeng Huang (Zhejiang University) and He Wang (State Oceanic Administration) for our guidance, and to thank Lanqing Huang (Shanghai Jiao Tong University) and Lin Ren (State Oceanic Administration) for helpful discussions and suggestions.

Author Contributions: Lei Wang and Bing Han conceived and performed the experiments. Bin Lei and Chibiao Ding gave the experimental revisions. Lei Wang drafted the manuscript. And all authors contributed to the discussion and revising of the manuscript.

Conflicts of Interest: The authors declare no conflict of interest.

References

1. Bergeron T, Bernier M, Chokmani K, et al. Wind Speed Estimation Using Polarimetric RADARSAT-2 Images: Finding the Best Polarization and Polarization Ratio[J]. IEEE Journal of Selected Topics in Applied Earth Observations & Remote Sensing, 2011, 4(4):896-904.
2. Zhang B, Perrie W, Vachon P W, et al. Ocean Vector Winds Retrieval From C-Band Fully Polarimetric SAR Measurements[J]. IEEE Transactions on Geoscience & Remote Sensing, 2012, 50(11):4252-4261.
3. Moon W M, Staples G, Kim D J, et al. RADARSAT-2 and Coastal Applications: Surface Wind, Waterline, and Intertidal Flat Roughness[J]. Proceedings of the IEEE, 2010, 98(5):800-815.
4. Yang X, Li X, Zheng Q, et al. Comparison of Ocean-Surface Winds Retrieved From QuikSCAT Scatterometer and Radarsat-1 SAR in Offshore Waters of the U.S. West Coast[J]. IEEE Geoscience & Remote Sensing Letters, 2010, 8(1):163-167.
5. Rivas M B, Stoffelen A, Zadelhoff G J V. The Benefit of HH and VV Polarizations in Retrieving Extreme Wind Speeds for an ASCAT-Type Scatterometer[J]. IEEE Transactions on Geoscience & Remote Sensing, 2014, 52(7):4273-4280.
6. Xu Q, Lin H, Li X, et al. Assessment of an analytical model for sea surface wind speed retrieval from spaceborne SAR[J]. International Journal of Remote Sensing, 2010, 31(4):993-1008.
7. Horstmann J, Koch W, Lehner S, et al. Wind retrieval over the ocean using synthetic aperture radar with C-band HH polarization[J]. IEEE Transactions on Geoscience & Remote Sensing, 2000, 38(5):2122-2131.
8. Plant W J. A two-scale model of short wind-generated waves and scatterometry[J]. Journal of Geophysical Research Oceans, 1986, 91(C9):10735–10749.
9. Romeiser R, Schmidt A, Alpers W. A three-scale composite surface model for the ocean wave–radar modulation transfer function[J]. Journal of Geophysical Research Oceans, 1994, 99(C5):9785-9801.
10. Romeiser R, Alpers W. An improved composite surface model for the radar backscattering cross section of the ocean surface: 2. Model response to surface roughness variations and the radar imaging of underwater bottom topography[J]. Journal of Geophysical Research Oceans, 1997, 102(C11):25251-25267.
11. Zou Q, He Y, Perrie W, et al. Wind-Vector Estimation for RADARSAT-1 SAR Images: Validation of Wind-Direction Estimates Based Upon Geometry Diversity[J]. IEEE Geoscience & Remote Sensing Letters, 2007, 4(1):176-180.
12. Escudero B, Diez A, Mart N A, et al. Scatterometer data interpretation: Estimation and validation of the transfer function CMOD4[J]. Journal of Geophysical Research Oceans, 1997, 102(C3):5767-5780.

13. Quilfen Y, Chapron B, Elfouhaily T, et al. Observation of tropical cyclones by high-resolution scatterometry. J. Geophys. Res. 103(C4), 7767-7786[J]. Journal of Geophysical Research Atmospheres, 1998, 103(C4):7,767-7,786.
14. Hersbach H, Stoffelen A, Haan S D. An improved C-band scatterometer ocean geophysical model function: CMOD5[J]. Journal of Geophysical Research Oceans, 2007, 112(C3).
15. Hersbach H. Comparison of C-Band Scatterometer CMOD5.N Equivalent Neutral Winds with ECMWF[J]. Journal of Atmospheric & Oceanic Technology, 2010, 27(4):721-736.
16. Monaldo F M, Thompson D R, Pichel W G, et al. A systematic comparison of QuikSCAT and SAR ocean surface wind speeds[J]. Geoscience & Remote Sensing IEEE Transactions on, 2004, 42(2):283-291.
17. Monaldo F, Thompson D. Implications of QuikSCAT and RADARSAT wind comparisons for SAR wind speed model functions[C]// Geoscience and Remote Sensing Symposium, 2002. IGARSS '02. 2002 IEEE International. IEEE, 2002:1881-1883 vol.3.
18. Yang X, Li X, Pichel W G, et al. Comparison of Ocean Surface Winds From ENVISAT ASAR, MetOp ASCAT Scatterometer, Buoy Measurements, and NOGAPS Model[J]. IEEE Transactions on Geoscience & Remote Sensing, 2011, 49(12):4743-4750.
19. Mouche A A, Hauser D, Daloze J F, et al. Dual-polarization measurements at C-band over the ocean: results from airborne radar observations and comparison with ENVISAT ASAR data[J]. IEEE Transactions on Geoscience & Remote Sensing, 2007, 43(4):753-769.
20. Rodrigues D F, Landau L, Junior A R T, et al. Sea Wind Extraction From RADARSAT-2 and Scatterometer Data Over the Gulf of Mexico[J]. IEEE Geoscience & Remote Sensing Letters, 2017, 14(7):1007-1011.
21. Monaldo F M, Thompson D R, Pichel W G, et al. Comparison of RADARSAT SAR-derived wind speeds with buoy and QuikSCAT measurements[C]// Geoscience and Remote Sensing Symposium, 2001. IGARSS '01. IEEE 2001 International. IEEE, 2001:1759-1760 vol.4.
22. Horstmann J, Koch W, Lehner S, et al. Coastal high-resolution wind fields retrieved from RADARSAT-1 ScanSAR[C]// Geoscience and Remote Sensing Symposium, 2001. IGARSS '01. IEEE 2001 International. IEEE, 2001:1747-1749 vol.4.
23. F. Monaldo, C. Jackson, X. Li, and W. G. Pichel, Preliminary evaluation of Sentinel-1A wind speed retrievals, IEEE [J]. Sel. Topics Appl. Earth Obs. Remote Sens., vol. 9, no. 6, pp. 2638–2642, Jun. 2016.
24. Thompson, D.R.; Elfouhaily, T.M.; Chapron, B. Polarization ratio for microwave backscattering from the ocean surface at low to moderate incidence angles. In Proceedings of the IEEE International Geoscience and Remote Sensing Symposium, Seattle,WA, USA, 6–10 July 1998; pp. 1671–1673.
25. Vachon, P.W.; Dobson, F.W. Wind retrieval from RADARSAT SAR images selection of a suitable C-band HH polarization wind retrieval model. Can. J. Remote Sens. 2000, 26, 2122–2131.
26. Monaldo F M, Thompson D R, Beal R C, et al. Comparison of SAR-derived wind speed with model predictions and ocean buoy measurements[J]. Geoscience & Remote Sensing IEEE Transactions on, 2002, 39(12):2587-2600.
27. Zhang, B.; Perrie, W.G.; He, Y.J. Wind speed retrieval from RADARSAT-2 quad-polarization images using a new polarization ratio model. J. Geophys. Res. 2011, 116, 1318–1323.
28. Mouche, A.A.; Hauser, D.; Daloze, J.F.; Guerin, C. Dual polarization measurements at C-band over the ocean: Results from airborne radar observations and comparison with ENVISAT ASAR data. IEEE Trans. Geosci. Remote Sens. 2005, 43, 753–769.
29. Wang H, Yang J, Mouche A, et al. GF-3 SAR Ocean Wind Retrieval: The First View and Preliminary Assessment[J]. Remote Sensing, 2017, 9(7):694.
30. Vachon P W, Wolfe J. C-Band Cross-Polarization Wind Speed Retrieval[J]. IEEE Geoscience & Remote Sensing Letters, 2011, 8(3):456-459.
31. Zhang B, Perrie W. Cross-Polarized Synthetic Aperture Radar: A New Potential Measurement Technique for Hurricanes[J]. Bulletin of the American Meteorological Society, 2011, 93(4):531-541.
32. Zhang B, Perrie W, Zhang J A, et al. High-Resolution Hurricane Vector Winds from C-Band Dual-Polarization SAR Observations[J]. Journal of Atmospheric & Oceanic Technology, 2014, 31(2):272-286.
33. Shen H, Perrie W, He Y, et al. Wind Speed Retrieval From VH Dual-Polarization RADARSAT-2 SAR Images[J]. IEEE Transactions on Geoscience & Remote Sensing, 2014, 52(9):5820-5826.
34. Hwang P A, Stoffelen A, Zadelhoff G J V, et al. Cross-polarization geophysical model function for C-band radar backscattering from the ocean surface and wind speed retrieval[J]. Journal of Geophysical Research Oceans, 2015, 120(2):893-909.

35. Horstmann J, Falchetti S, Wackerman C, et al. Tropical Cyclone Winds Retrieved From C-Band Cross-Polarized Synthetic Aperture Radar[J]. IEEE Transactions on Geoscience & Remote Sensing, 2015, 53(5):2887-2898.
36. Huang L, Liu B, Li X, et al. Technical Evaluation of Sentinel-1 IW Mode Cross-Pol Radar Backscattering from the Ocean Surface in Moderate Wind Condition[J]. Remote Sensing, 2017, 9(8):854.
37. Horstmann J, Lehner S. A new method for radiometric calibration of spaceborne SAR and its global monitoring[C]// Geoscience and Remote Sensing Symposium, 2002. IGARSS '02. 2002 IEEE International. IEEE, 2002:620-622 vol.1.
38. Stoffelen A. A Simple Method for Calibration of a Scatterometer over the Ocean[J]. Journal of Atmospheric & Oceanic Technology, 2010, 16(2):275-282.
39. Verspeek J, Stoffelen A, Verhoef A, et al. Improved ASCAT Wind Retrieval Using NWP Ocean Calibration[J]. IEEE Transactions on Geoscience & Remote Sensing, 2012, 50(7):2488-2494.
40. Zhu J, Dong X, Yun R. Calibration and validation of the HY-2 scatterometer backscatter measurements over ocean[J]. 2014(IGARSS):4382-4385.
41. Sun, J.L.; Yu, W.D.; Deng, Y.K. The SAR payload design and performance for the GF-3 mission. Sensors 2017,17, 2419
42. Shao W, Sheng Y, Sun J. Preliminary Assessment of Wind and Wave Retrieval from Chinese Gaofen-3 SAR Imagery.[J]. Sensors, 2017, 17(8).
43. Ren L, Yang J, Mouche A, et al. Preliminary Analysis of Chinese GF-3 SAR Quad-Polarization Measurements to Extract Winds in Each Polarization[J]. Remote Sensing, 2017, 9(12):1215.
44. Wang H, Wang J, Yang J et al. Empirical Algorithm for Significant Wave Height Retrieval from Wave Mode Data Provided by the Chinese Satellite Gaofen-3[J]. Remote Sensing, 2018, 10(3), 363.
45. Shao W, Yuan X, Sheng Y, et al. Development of Wind Speed Retrieval from Cross-Polarization Chinese Gaofen-3 Synthetic Aperture Radar in Typhoons[J]. Sensors, 2018, 18(2).
46. Chang Y, Li P, Yang J, et al. Polarimetric Calibration and Quality Assessment of the GF-3 Satellite Images[J]. Sensors, 2018, 18(2):403.
47. Horstmann J, Schiller H, Schulz-Stellenfleth J, et al. Global wind speed retrieval from SAR[J]. Geoscience & Remote Sensing IEEE Transactions on, 2003, 41(10):2277-2286.
48. ECMWF ERA-Interim Daily. Available online: http://apps.ecmwf.int/datasets/data/interim-full-daily/levtype=sfc/
49. Hawkins R, Attema E, Crapolicchio R, et al. Stability of Amazon Backscatter at C-Band: Spaceborne Results from ERS-1/2 and RADARSAT-1.[J]. 1999, 450:99.